THE PENNSYLVANIA STATE UNIVERSITY
SCHREYER HONORS COLLEGE

DEPARTMENT OF CHEMISTRY

SELECTIVE LIGHT SCATTERING FROM A SILICA-PMMA COMPOSITE

LELAND C. SMITH
Spring 2010

A thesis
submitted in partial fulfillment
of the requirements
for a baccalaureate degree
in Chemical Engineering
with honors in Chemistry

Reviewed and approved* by the following:

Thomas Mallouk
DuPont Professor of Materials Chemistry and Physics
Thesis Supervisor

Karl Mueller
Professor of Chemistry
Honors Adviser

Andrew Zydney
Professor of Chemical Engineering
Department Head

* Signatures are on file in the Schreyer Honors College.

Abstract

A dispersion of silica nanoparticles in Poly (methyl methacrylate) (PMMA) is investigated as a potential lens material for a hybrid solar cell. PMMA is polymerized from methyl methacrylate (MMA) to make optically clear cylinders one inch in diameter. Spherical silica particles 274nm, 350nm and 600nm in diameter are surface treated using 3-(trimethoxysilyl)propyl methacrylate, dispersed in MMA, and polymerized into the polymer matrix using benzoyl peroxide initiator. The resulting silica-PMMA composites are cylinders one inch in diameter and appear homogenous. UV-visible spectroscopy is used to measure the transmittance of the silica-PMMA composites. Also, thin films of germanium and titanium-doped silica are deposited onto microscope slides and the refractive index of these films is estimated from reflectance measurements taken with UV-visible spectroscopy.

Table of Contents

Acknowledgements

I would like to thank Dr. Tom Mallouk and all of the members of the Mallouk group for their support and friendship over the last two years. In particular, I thank Dr. Greg Barber for his guidance and encouragement in all facets of this project.

I.   Introduction

    A. Solar Cell Efficiency

Efficiency is a key metric for measuring solar cell performance.   There are many ways of

calculating solar cell efficiency, but the energy conversion efficiency (η) is most frequently

reported:

$$\eta = \frac{P_m}{E \times A_c}$$

    (1)

P_m is the maximum power produced by the cell, E is the irradiance under standard test

conditions, and A_c is the surface area of the cell. Irradiance is measured in suns, where one sun
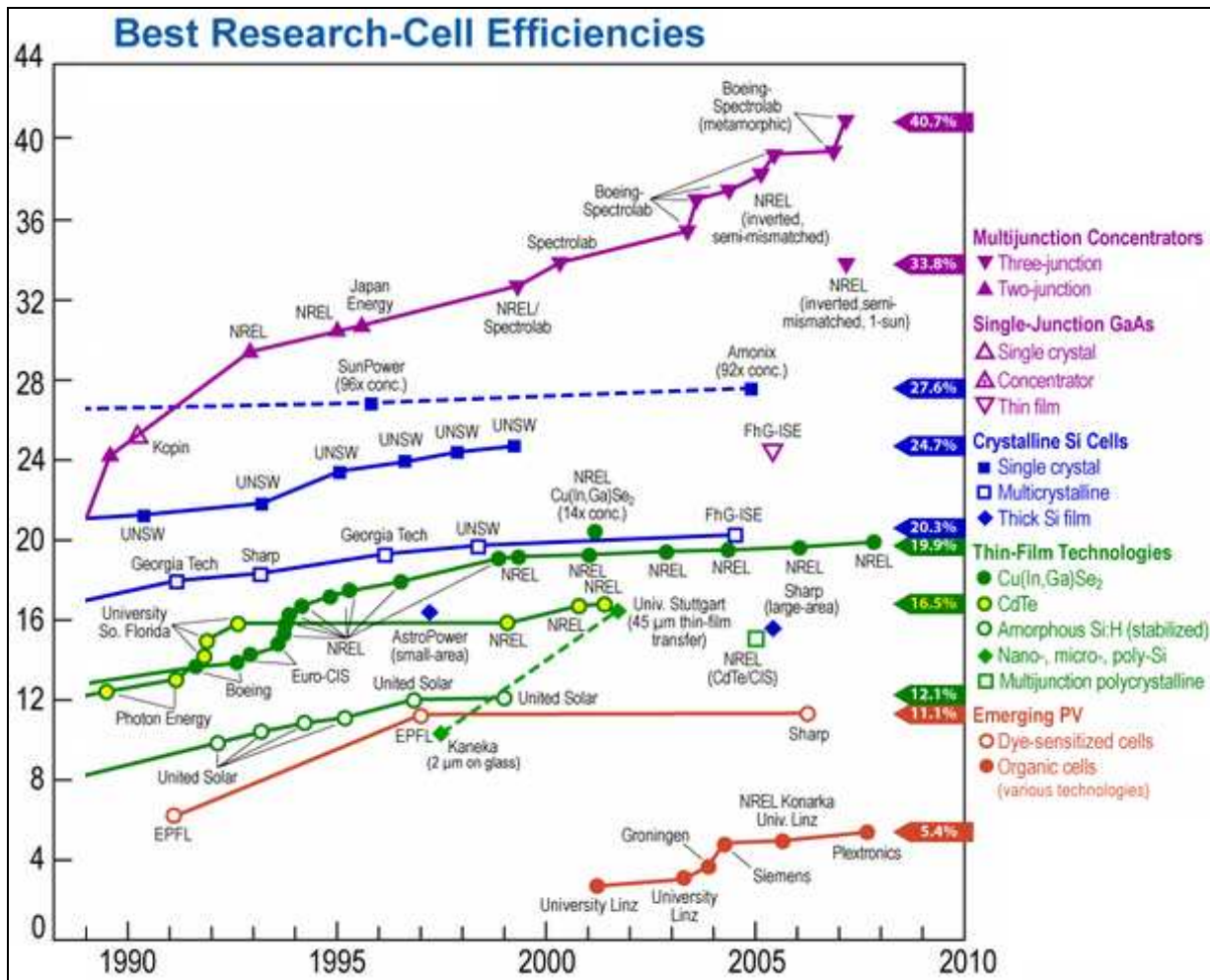

Figure 1: trends in solar cell efficiencies achieved at various research centers over twenty years

is equivalent to 1000 W/m^2 with an air-mass of 1.5. The efficiency of most solar cells can be increased by concentrating the incident sunlight beyond one sun.

Figure 1 shows the trends in energy conversion efficiency for a variety of solar cells over the last twenty years.[1] The highest efficiencies are seen in multi-junction cells produced for space applications and solar concentrators. Most solar panels deployed today are single-junction silicon or thin films. These technologies have research efficiencies of between 19-25%. Emerging solar cells have relatively low efficiencies, but are of interest for their low production costs compared to silicon and thin-films.

To determine where efficiency gains can be made, it is necessary to understand how solar cells generate current. The photovoltaic effect is produced by a layered arrangement of doped semiconductors called a p-n junction (Figure 2)[2]. In silicon cells phosphorous is used as a negative dopant (n-doped) because it has 5 valence electrons, one more than silicon. Boron, with three valence electrons, is used as a positive dopant (p-doped).
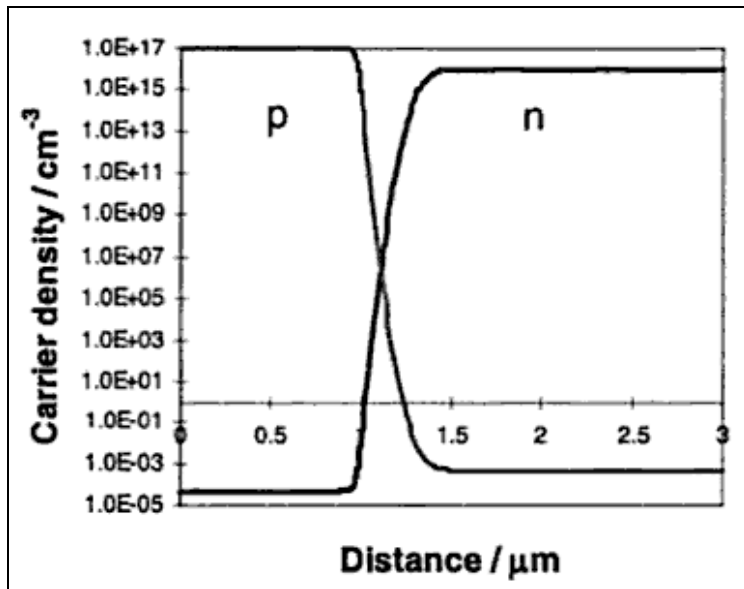

Figure 2: The densities of positive and negative charge carriers at equilibrium as a function of distance from the positive electrode. Near the p-n junction (D=1.2μm) the carriers annihilate.

When the p-n junction is not exposed to sunlight or any electrical bias, it is at equilibrium. Electrons and holes at the p-n interface annihilate, leaving that region depleted of free carriers. When electrons are annihilated in the n-doped region positive charge is left behind, and conversely when holes are annihilated in the p-type region negative charge is left behind.

This depletion of carriers creates an electric field within the space charge region. When a p-n junction is exposed to sunlight, valence band electrons in the space charge region become excited and conduct across the interface, through the n-doped region and through an external circuit. As the electrons conduct from the interface they leave behind holes which are conducted through the p-doped region and ultimately recombine with electrons that travel through the external circuit.

The potential difference that exists across the space charge region is called the band gap energy (E_{gap}) and determines how a p-n junction will be affected by an incoming photon. If an incident photon has less than E_{gap}, the photon will not be absorbed by the semiconductor. If the photon has at least E_{gap}, it will create an electron-hole pair within the p-n junction and current will be produced. If the photon energy exceeds E_{gap}, the extra energy will be lost as heat.[2] Take for example, a silicon cell exposed to the solar spectrum at sea level (Figure 3)[3]. For the cell to be 100% efficient, it would have to produce electrical power equal to all of the red area in Figure
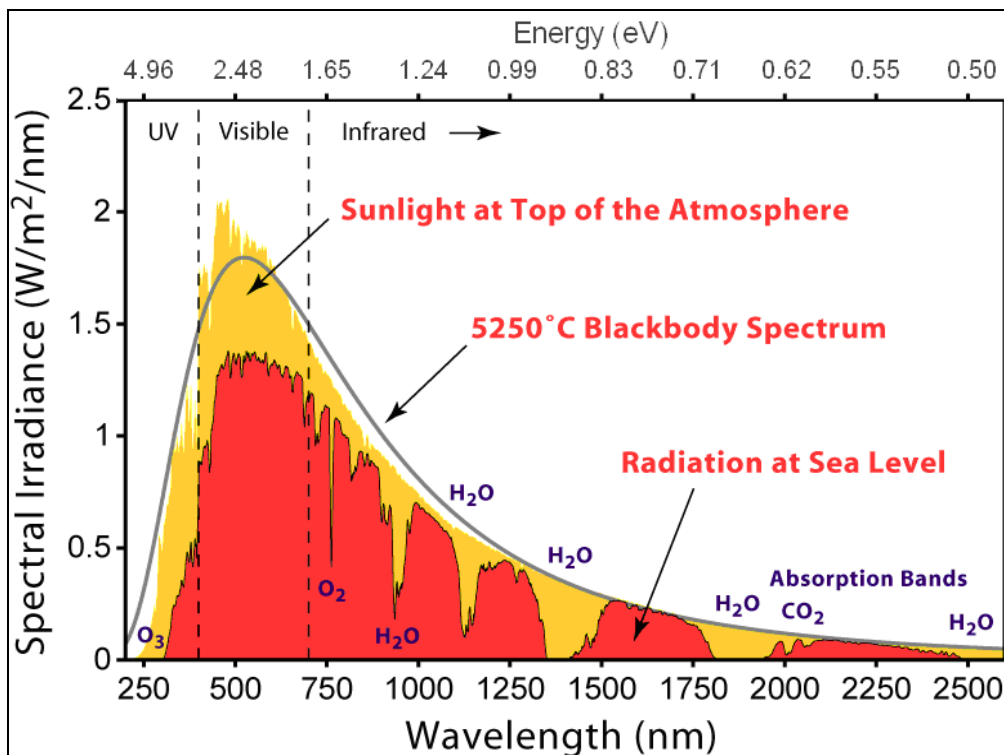

Figure 3: Solar irradiance in wavelength(nm) and photon energy(eV)

3. However, silicon has $E_{gap} = 1.1eV = 1100nm$, so any light with E<1.1eV will not produce current and any light with more than 1.1eV will produce current at only 1.1eV. These facts place a physical limit on the efficiency of a single junction solar cell, known as the Shockley-Queisser limit. For a single junction silicon cell without concentration, the Shockley-Quiesser limit is 31% efficiency.[4] The best single junction silicon cells are currently about 22% efficient. The other 9% loss in efficiency can be attributed to issues such as mismatch with the solar spectrum, the fact that silicon is an indirect gap semiconductor, material defects, surface reflectance, and temperature dependent performance. Still the majority of photovoltaic efficiency losses stem from the fundamental physics of the p-n junction.

While efficiency is an important metric for device performance, the cells with the highest efficiency are not the most widely deployed in residential and utility-scale photovoltaic installations. The extent of cell deployment is more easily predicted by comparing the electrical power produced by a panel to the total cost of owning the panel. This metric is known as price per watt. Price per watt depends on a number of factors such as cell efficiency, production costs, installation and maintenance costs, geography, etc. Depending on the application, different types of solar cells will be cheapest per watt. For example, the solar panels deployed on the International Space Station are triple junction Gallium Arsenide (GaAs) cells that are 28.3% efficient under one sun illumination and air-mass zero.[5] These cells are extremely expensive to manufacture, but they are used for space applications because the cost of manufacturing is far outweighed by the cost of transporting and installing the panels in orbit. For terrestrial solar applications, production costs are much more significant. Currently, single-junction silicon and thin-film photovoltaics produce electricity for about $5/watt compared to $0.40/watt for a gas-fired power plant.[6] Solar cells compete in large part due to government policy. To accelerate the growth of solar power and assure its long-term viability, scientists and engineers must develop solar technologies that beat the price of fossil fuels. This can only be

accomplished by increasing solar cell efficiency while limiting production costs.

A. Multiple Band Gap Solar Cells

To produce big gains in solar cell efficiency, it is necessary to overcome the physical limitations specified by the Shockley Quiesser efficiency.   Cells that have multiple band gaps can convert more of the solar spectrum to electrical current. As demonstrated in Figure 4, it is possible to produce semiconductors with band gaps throughout the range of the solar spectrum.[4]

Figure 4: the band gaps of semiconductors are distributed throughout the solar spectrum
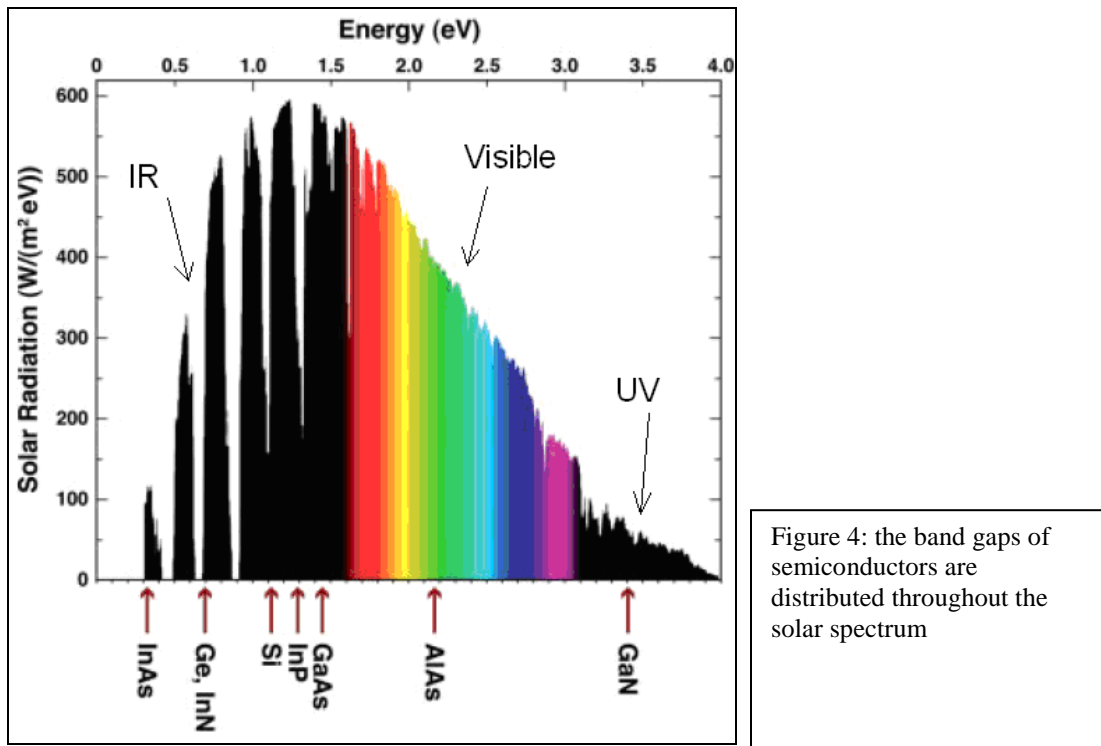
There are several strategies for building solar cells with multiple band gaps. One class of multi-band gap solar cells that was already mentioned is multi-junction cells. These are made by stacking layers of p-n junctions optically and electrically in series. The top layer has the highest band gap energy and absorbs the violet end of the solar spectrum. Subsequent layers absorb lower energy (longer wavelength) radiation. Because the layers are electrically in series, the current produced by a multi-junction cell is limited to the lowest current junction.

Another type of multi-band gap solar cell is the intermediate-band cell. In a typical single junction cell, electrons absorb the band gap energy and move from the semiconductor's valence band to its conduction band. Intermediate-band cells use a single junction, but have impurities (typically quantum dots) deposited into the semiconductor. These impurities provide a mid-point for electrons between the valence and conduction bands, called an intermediate band. This intermediate band helps convert sub-band gap light into current and thereby increases the fraction of the solar spectrum accessible to a single-junction cell. Intermediate-band cells are a much newer technology than multi-junction cells and currently have lower overall efficiency than single-junction cells. Still, experiments have confirmed the existence of intermediate bands and demonstrated their ability to absorb sub-band gap photons.[4]

Hot carrier cells are yet another possible (but still unrealized) technology for increasing the efficiency of single-junction solar cells beyond the Shockey Quiessler limit. Hot carrier cells are similar to intermediate-band cells except that rather than harness photons below Egap, hot carrier cells collect more than Egap from high energy photons, effectively giving the device a second, higher band gap. Instead of allowing an excited electron to lose energy to heat, hot carrier cells use that energy to excite a second electron into the conducting band. Like intermediate-band cells, designs for hot carrier cells involve the use of microstructures like quantum dots or highly mismatched alloys. Hot carrier cells are still in the early stages of research and cannot compete with the efficiency of traditional single-junction cells.

The hybrid solar cell is another design for multiple band gap absorption and is the specific interest of this report. Like multi-junction cells, a hybrid arrangement features two or more independent solar cells with different band gap energies. Unlike multi-junction cells, hybrid cells have p-n junctions arranged both optically and electrically in parallel. For such a cell to work, a material is required that can separate the solar spectrum into bins, where each bin is centered on the band gap of a certain type of solar cell. For the dye-sensitized solar cell

(DSSC)/silicon hybrid the solar spectrum should be separated around $\lambda=650$nm with the longer

wavelengths directed toward the silicon cell and the shorter wavelengths directed toward the

DSSCs.

C. Silicon-DSSC Hybrid

Dye Sensitized Solar Cells (DSSC) are among the 'emerging technologies' listed in

Figure 1. DSSCs are an attractive alternative to current solar technologies because they are made

of relatively inexpensive materials. However, the maximum experimental efficiency for a DSSC

is only 11%. In DSSCs, charge separation occurs in the dye and electrons are conducted through

the titania (TiO_2). While many different dyes are used, they all have fairly low absorbance in the

IR spectrum ($\lambda>650$nm). Whereas a DSSC is only 8-10% efficient in the full spectrum, they are

about 20-25% efficient in the visible (400-650nm) spectrum.[7]

As shown previously (Figure 4), the band gap of silicon is 1.1eV, meaning silicon p-n

junctions operate most efficiently near $\lambda=1100$nm. Considering the good performance of

DSSCs in the visible and the efficient operation of silicon in the red and IR, researchers were

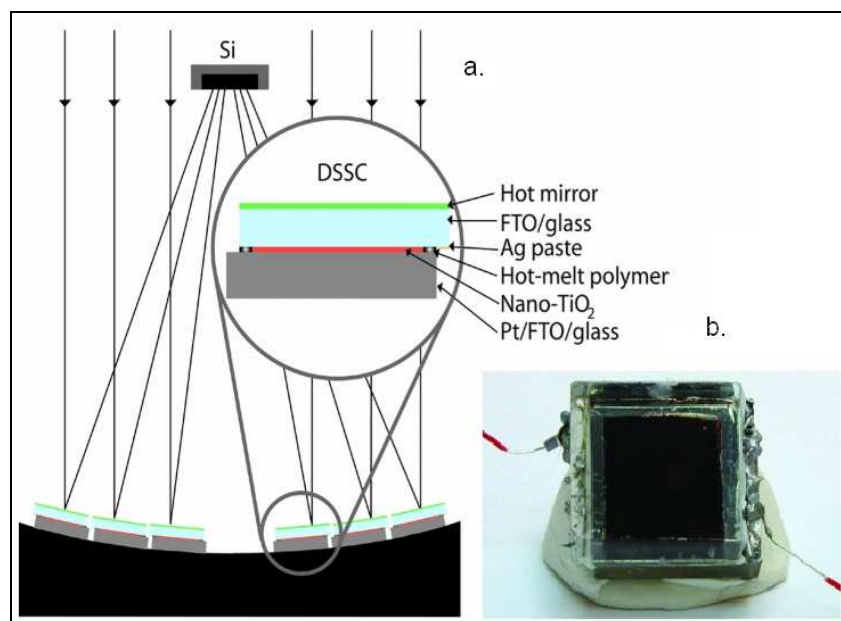motivated to combine these two cells in a hybrid arrangement.[7] Figure 5b is a picture of the

Figure 5: a diagram silicon/DSSC hybrid with light separation created by a hot-mirror lens (a.) and a photograph of the 14.5% efficient silicon/DSSC hybrid cell (b.)

first silicon-DSSC hybrid cell constructed by members of the Mallouk Group. The DSSCs are covered with hot mirrors that selectively reflect $\lambda > 650nm$. Each DSSC is on a slight angle, creating a parabolic dish that concentrates these wavelengths onto the silicon cell. The hybrid cell in Figure 5 paired an 8.6% efficient DSSC with an 18.1% efficient silicon and achieved an overall cell efficiency of 14.5%. Not only does the hybrid design split the solar spectrum, it also concentrates the near-IR light onto the silicon cell, thus achieving efficiency gains. The silicon accounts for just 16.5% of the active surface area of the cell, but it receives 62% of the incident power. One shortcoming of this design is that the hot mirrors are very expensive. Also, the inverted silicon cell blocks a significant portion of the incoming radiation.

An alternative design that may solve these issues is to build a totally flat cell and direct light using a hemispherical lens. Unlike the hot-mirror design, the spectrum is not separated and directed via reflectance, but through scattering caused by small particles embedded in the lens. The lens could be made of poly (methyl methacrylate), an optically clear, lightweight and rigid polymer and the particles could be made of cheap inorganic materials like silica, germania, titania, etc.

II.   Theory

        A. Geometry

The hybrid lens design is hemispherical (half cylinder) with the curved face upward to the sun and the flat face contacting the solar cells. The solar panels are arranged so that the sun tracks across the circumference of the lenses (Figure 6b). The lens should be ~2 inches
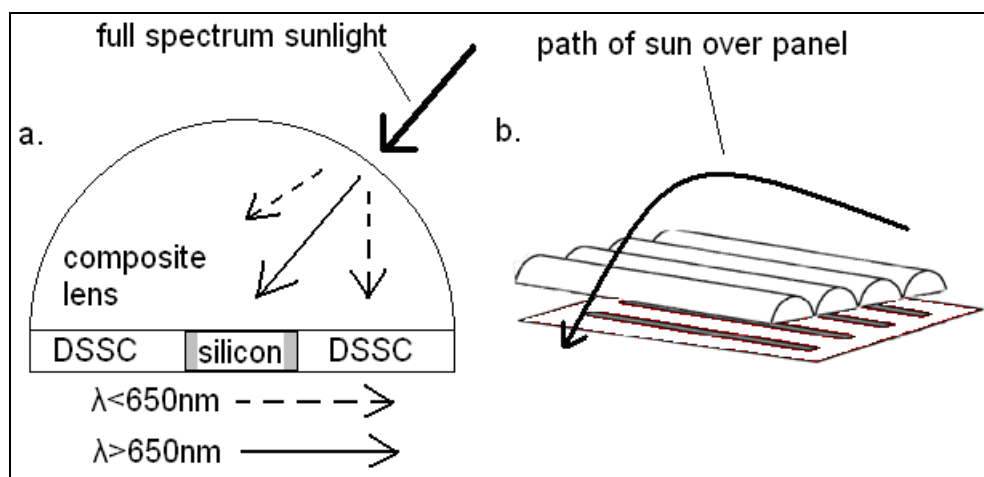

Figure 6: the lens separates the solar spectrum through selective scattering λ<650nm and concentrates λ>650nm onto the silicon cell (a.) the lenses should be arranged perpendicular to the path of the sun (b.)

in diameter to provide ample room for the solar cells underneath. Unlike the hot mirror, the lens allows the silicon cell and DSSC to lie in the same plane, both facing upwards. Figure 6a is a basic sketch of the scattering phenomena needed to make the hybrid lens work. The shorter wavelengths (<650nm) forward scatter toward the DSSCs, while the longer wavelengths (>650nm) do not scatter and pass directly to the silicon cell. Like the hot-mirror arrangement, the hemispherical lens concentrates longer wavelengths onto the silicon cell. Producing the selective scattering shown in Figure 6a is complex problem and is the main challenge addressed in this thesis. Scattering depends on numerous variables and is described by a number of mathematical models.

A. Scattering Parameters

There are two essential criteria for the hybrid lens. First, the hybrid lens should forward scatter light in the region of λ<650nm (blue light) so that these wavelengths are directed toward the DSSCs. Forward scattering should predominate because backscattering will decrease the flux of sunlight to the solar cells. Second, the lens should only minimally scatter light with λ >650nm (red light). These wavelengths should pass unperturbed to the silicon cell.

There are many variables that affect how particles embedded in a polymer will scatter light. These variables include: wavelength (λ) of the light, indices of refraction (n) of the particles and the polymer, the size and shape of the particles, the degree of aggregation of particles, and the distance between individual particles. To evaluate scattering phenomena, it is helpful to limit the number of variables in the system.

Several simplifying assumptions can be made to shorten the list of important variables. By only considering spherical particles it is not necessary to account for the orientation of the particles. Furthermore, spherical particles can be described with one size variable, diameter (d). It is also useful to assume that the particles are homogeneously dispersed (i.e. no clumping). This vastly simplifies the theory of scattering, though making truly homogenous dispersions in the lab is difficult.   The distance between scattering particles is called the mean free path.

$$\ell = (\sigma n)^{-1}$$
(2)

Here ℓ is the mean free path, σ is the cross-sectional area of scatterers and n is the number of scatterers per volume. If ℓ is large enough, each particle can be assumed to scatter independently of its neighbors. While any given photon will be scattered by many particles as it passes through polymer, independent scattering requires that each scattering event be caused by only one particle. Estimates suggest that ℓ must be at least three times the wavelength of light for independent scattering to hold.[8] The composites studied in this report have ℓ several hundred times larger than the wavelength of light, so scattering events should be independent.

With these assumptions made, there are four remaining variables needed to describe scattering phenomena. They are the diameter (d), wavelength (λ), and indices of refraction (n) of the polymer and the particle. Index of refraction describes how quickly light of a certain wavelength propagates through a material. The wavelength dependence of n is shown on a plot called a dispersion curve. Figure 7 shows the dispersion curves for PMMA and silica.[9]
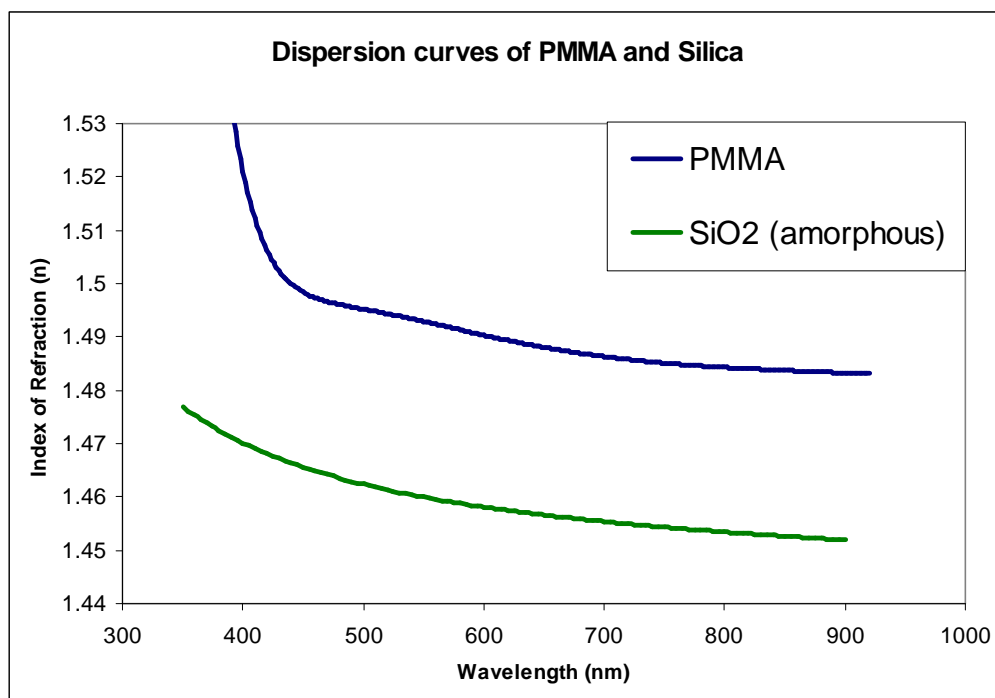

Figure 7: Dispersion curves for silica and PMMA display relatively constant Δn.

While a rigorous calculation of scattering requires absolute values of n for both particle and polymer, scattering is largely dependent on the difference between the two indices (Δn). As light propagates between materials with different n, it will change speed. Large Δn causes scattering and reflection. As Δn approaches zero light is scattered less. If two materials have identical indices ($\Delta n=0$) light behaves the same way in both, and no scattering will occur between the materials.

With the dispersion curves above, scattering theory can be applied to the SiO2-PMMA system to determine what particle size will cause forward scattering for $\lambda<650nm$. This satisfies the first criterion for the lens and is the topic of Section C. The second criterion, that $\lambda>650nm$

not scatter, motivates a discussion of index matching in Section D.

C. Forward Scattering

The simplest model of particle scattering is Rayleigh scattering, which assumes that the scattering particles are much smaller than the wavelength of light. The Rayleigh equation

$$I = I_0 \underset{1}{\frac{1 + \cos^2 \theta}{2R^2}} \underset{2}{\left(\frac{2\pi}{\lambda}\right)^4} \underset{3}{\left(\frac{n^2 - 1}{n^2 + 2}\right)^2} \underset{4}{\left(\frac{d}{2}\right)^6}$$

(3)

describes the intensity (I) of the light of a certain wavelength (λ) that is scattered in a direction (θ). The particles are assumed to be suspended in air ($n_{air}=1$). For a particle with a certain diameter (d) and constant n, the third and fourth terms are constant at all wavelengths so intensity is dependent only on scattering angle and wavelength. The λ-dependence of the second term shows that shorter wavelengths are scattered more strongly than longer wavelengths. Rayleigh scattering correctly predicts the blue color of the sky. Gases in the upper atmosphere fluctuate in density, behaving like very small scattering particles. Blue is scattered more strongly than red, so the sky appears predominately blue from the earth's surface.

Blue light is scattered more strongly than red in the Rayleigh regime, which is a requirement for the hybrid lens. However, in the first term of Equation 3 scattering intensity is proportional to $(1 + \cos^2 \theta)$. By convention the angle of scattering is 0° for light that is scattered directly forwards and 180° for light that gets scattered directly back. The $(1 + \cos^2 \theta)$ dictates that there will be a maximum in I at 0° and 180°. Therefore, light will be scattered forward and backward with equal intensities. This is unacceptable for the hybrid lens because all of the backscattered light would not reach the solar cells. It is therefore necessary to investigate scattering from larger particles.

The simple equation of Rayleigh does not apply to larger scatterers. Rayleigh theory is derived from Maxwell's Equations using the simplification that when a small particle scatters

light, it will experience an instantaneous and uniform electiric field.[8] For particles of size comparable to the wavelength of light this simplification cannot be made and a full solution of Maxwell's Equations is required. Such a solution is called Mie theory, named for Gustav Mie who was among the first physicists to tackle this problem. The Mie calculations in this report were made using an online Mie Scattering Calculator provided by the Oregon Laser Medical Center.[10]

The Mie solution for small particles demonstrates equal forward and backward scattering, which is characteristic of Rayleigh theory. Figure 8 shows a scattering profile for 10nm spherical silica particles in PMMA. Light of λ=450nm propagates across the horizontal axis from 180° to 0° and the particle is located at the origin. The polar scattering diagram is marked
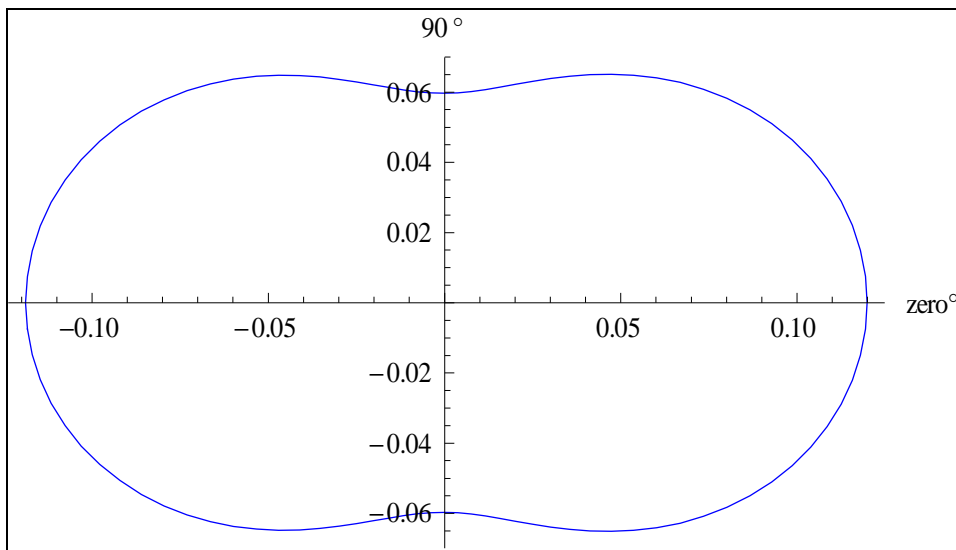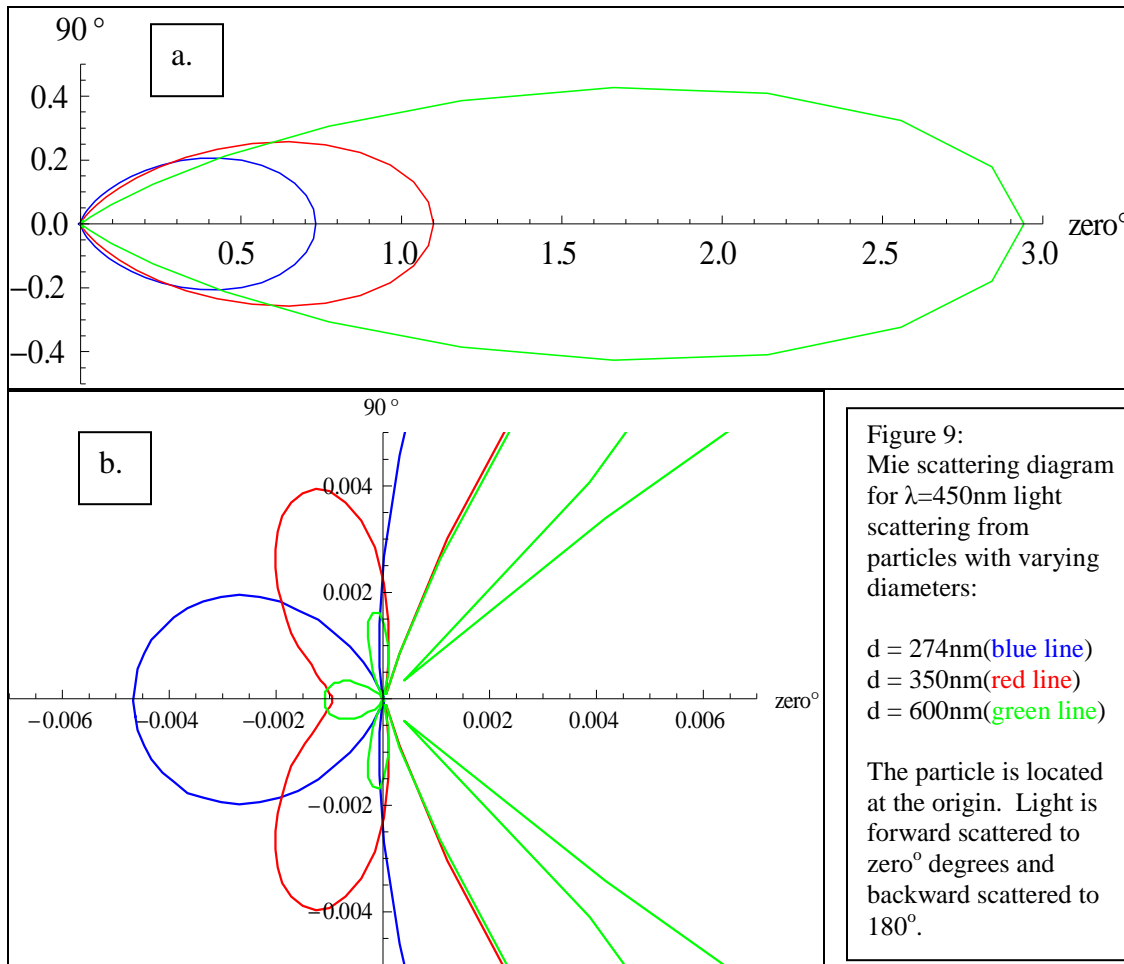

Figure 8: Mie scattering profile for a 10nm particle in PMMA

with relative intensities, which show the large degree of backward scattering.

As particle size increases, the scattering pattern becomes biased forward. Figure 9 shows scattering diagrams for larger silica particles in PMMA scattering λ=450nm light. This is a good wavelength to evaluate scattering because it is the point of maximum energy flux in the solar spectrum. For the hybrid lens to achieve efficiency gains, wavelengths around 450nm must be scattered almost entirely forward. Figure 9a shows the full scattering diagram for scattering

from particles with diameters: 274nm (blue line), 350nm (red line) and 600nm (green line).

There are several trends evident in this data. Larger diameter particles scatter forward

Figure 9:
Mie scattering diagram for λ=450nm light scattering from particles with varying diameters:

d = 274nm(blue line)
d = 350nm(red line)
d = 600nm(green line)

The particle is located at the origin. Light is forward scattered to zero° degrees and backward scattered to 180°.
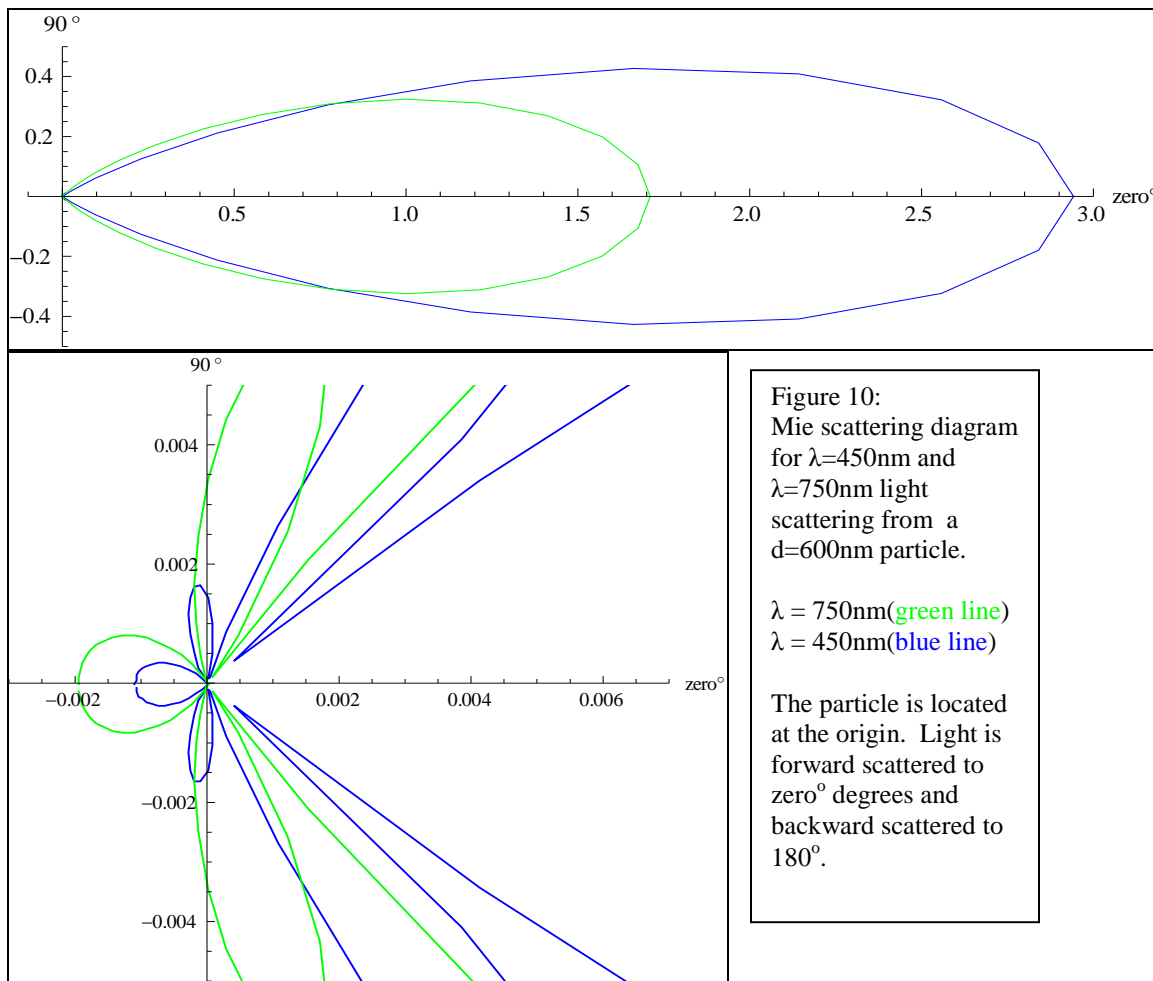
with stronger intensity. Also, larger particles scatter 450nm light in a smaller angle range. A

larger scattering cone could produce better color separation. However, too wide a scattering

angle could, over multiple scattering events, scatter some light away from the solar cells and out

of the lens. As is evident in Figure 9b, the larger particles scatter significantly less light

backwards. Thus, the 600nm particle appears to best meet the criteria of the hybrid lens.

Diameter in nanometers is not the most meaningful measure of particle size. It is more

logical to consider particle diameter with respect to the wavelength of light that is passing

through it. Light travels slower through materials with a higher index of refraction, while its

frequency stays constant. Thus the wavelength of light decreases in a higher index material

according to Equation 4:

$$\frac{\lambda^\circ}{\lambda} = \frac{f * c}{f * v} = n \tag{4}$$

The variables in Equation 4 are wavelength of light in a material and vacuum (λ and λ°), frequency (f), speed of light in a material and vacuum (v and c) and the index of refraction of the material, n. Silica has n=1.46, so light with λ=450nm in vacuum (or air) will have λ=308nm in silica. The d=600nm particle evaluated in Figure 9 is approximately two wavelengths in diameter with respect to light with λ==308nm in silica.

For longer wavelengths of light particles behave as if they are relatively smaller. Figure 10 compares the scattering intensity for 450nm and 750nm light traveling through 600nm silica. When exposed to λ=750nm light the d=600nm particle backscatters more and forward scatters across a larger angle range. These trends were characteristic of smaller particles in Figure 10.

Figure 10:
Mie scattering diagram for λ=450nm and λ=750nm light scattering from a d=600nm particle.

λ = 750nm(green line)
λ = 450nm(blue line)

The particle is located at the origin. Light is forward scattered to zero$^\circ$ degrees and backward scattered to 180°.

Assuming a relatively constant Δn (as in the SiO2-PMMA composite), a particle that is optimized to forward scatter in the blue range will backscatter at longer wavelengths, thereby decreasing the flux to the solar cell. The hybrid lens design requires that λ>650nm not scatter, but there is no way to accomplish this by adjusting particle diameter alone. A particle material is needed that will match the index of PMMA (Δn~0) for λ>650nm and not match for λ<650nm.

   D. Index Matching

   The silica-PMMA system has a relatively constant Δn across the visible spectrum. It may be possible to dope silica with a different optical material, giving doped silica a dispersion curve closer to that of PMMA. Composites of index-matched glass fibers in PMMA have been made with high transmittance. Olson et al concluded that index matching on the order of +/- 0.010n was needed to allow transmittance above 70% across the solar spectrum.[11] Similar experiments achieved transmittance above 80% across the solar spectrum.[12] To achieve 95% transmittance for red wavelengths, closer index matching is needed. The glass fiber composites were made for mechanical strength and were not optimized for forward scattering. Therefore closer index matching should be feasible.

   Figure 11 shows dispersion curves for various dopings of germania (GeO_2) in silica (SiO_2). The index of refraction for the doped-materials is calculated from a weighted average of published n data for pure GeO_2 and SiO_2.[9] Such an analysis assumes that germanium atoms are equally distributed in SiO_2 and have a uniform contribution to index. This assumption provides a
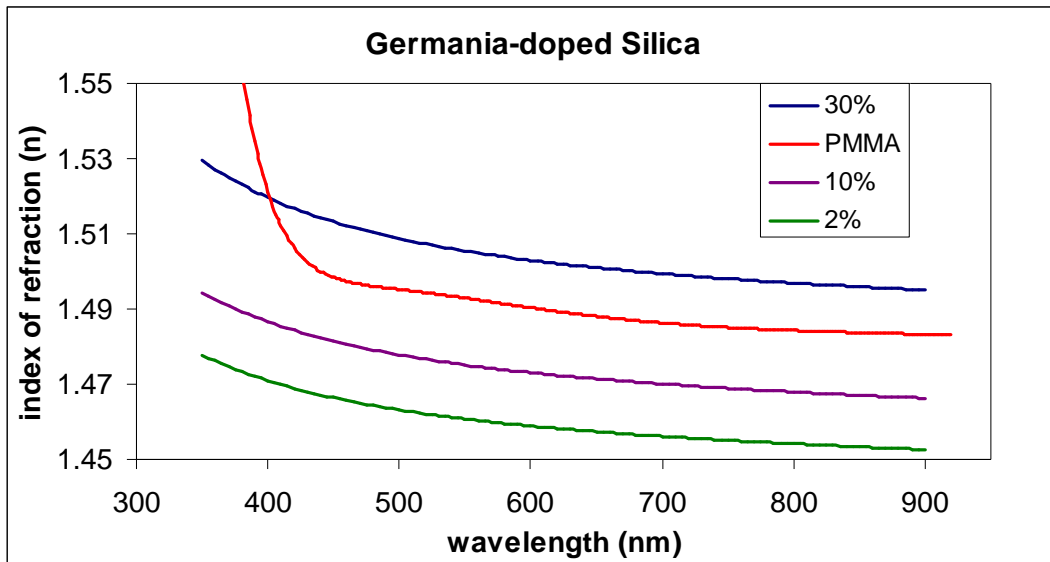
Figure 11: Weighted averages of germania and silica n data used to estimate the dispersion curves of silica doped with various mole % germania.

starting point to compare with experimental data.

Another potential dopant is titania (TiO_2). Theoretical dispersion curves for titania-doped silica are shown in Figure 12. It is evident that titania has a much higher index of refraction than silica as 10% titania causes a much larger increase in the index of doped silica than 10%
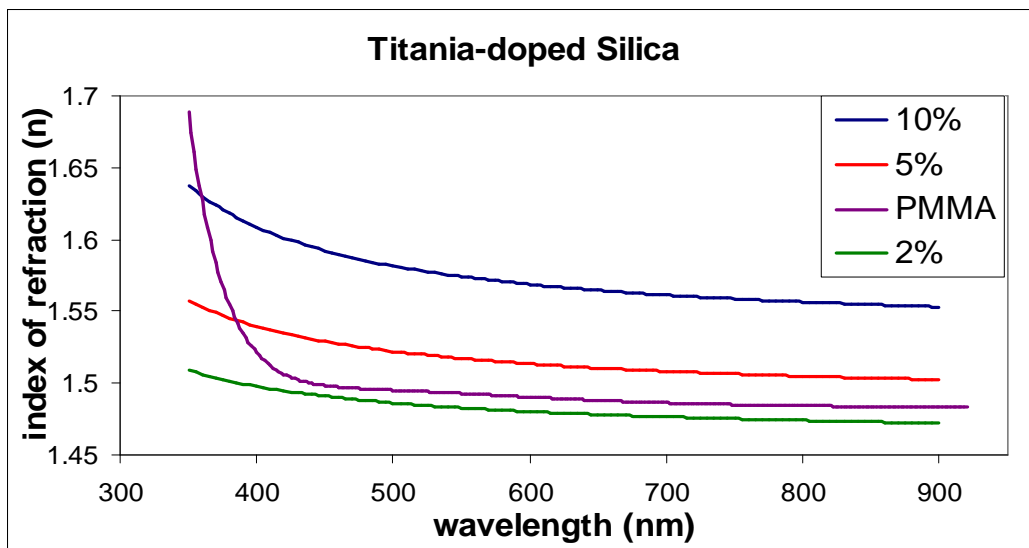

Figure 12: Weighted averages of titania and silica n data used to estimate the dispersion curves of silica doped with various mole % titania.

germania. It is also interesting to note the increasing downward slope in the titania-doped
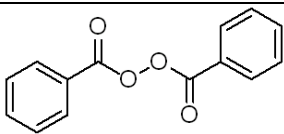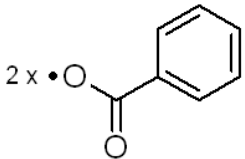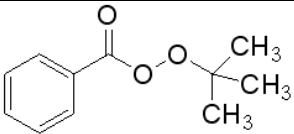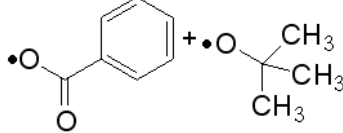
dispersion curve around 400nm. While pure germania has a relatively flat dispersion curve (n~1.63) across the visible spectrum, pure titania changes drastically from n=2.9 at λ=400nm to n=2.5 at λ=900nm. The variation in the shape of the dispersion curves between materials suggests that by doping several materials into silica, the refractive index could be fine-tuned to match PMMA in some part of visible spectrum. There are technical difficulties in making such particles (phase-separation, crystal structure, oxide deposition rates), but these issues could be addressed by making core-shell particles. A good starting point for index matching PMMA is to add germania to silica until it is closely matched across the spectrum. At that point, small amounts of titania could be added to create index separation in for λ<650nm.

III.   Experimental

A. Neat Polymer

Before making silica-PMMA composite samples a procedure was developed for making

thick samples of optically clear PMMA. Making large samples of PMMA that were free of

voids and bubbles proved difficult. PMMA is made via free-radical polymerization of methyl

methacrylate (MMA). In this process an initiator is mixed into the MMA sample. When the

mixture is heated, the initiator breaks down into two radicals which push their free electrons into

the π-system of a monomer creating a longer radical. The reaction propagates as the radical

donates an electron to other free monomers and the chain grows bigger. Some initiators are

more stable than others and require higher temperatures to dissociate and drive polymerization.

The balance between temperature, pressure and initiator determines whether a polymer

sample will be bubble free. Table 1 lists the three initiators that were investigated for the

polymerization of MMA: benzoyl peroxide (BPO), Azobisisobutyronitrile (AIBN), and tert-

Butyl peroxybenzoate (Luperox P). Initial tests were conducted polymerizing 10g of MMA with

Table 1: Free radical initiators investigated for the polymerization of MMA		
Initiator	Structure	Radical
benzoyl peroxide (BPO)		
azobisisobutyronitrile (AIBN)		
tert-Butyl peroxybenzoate (Luperox P®)		

between 0.5% and 1.6% AIBN in a 20ml scintillation vial (1 inch diameter) at 60$^{\text{o}}$C. Between

30 and 60min into these tests, bubbles would evolve from the sample. Some would rise to the

surface of the polymerizing mass and enter the headspace in the vial. Many bubbles would

remain suspended in the bulk. The pressure in the headspace sometimes got high enough to push

off the top of the vial. The stoichiometry of AIBN shows that for every mole of AIBN that

degrades a mole of N_2 is produced. This added gas was creating problems, so AIBN was

abandoned. BPO is another very common initiator for free-radical polymerization. Experiments

conducted with 2% weight BPA in MMA at 40$^{\text{o}}$C overnight produced mostly clear samples.

Also, experiments with 2.4% weight Luperox P at 50$^{\text{o}}$C overnight produced clear samples.

Polymerizing in the scintillation vials was unreliable as bubbles would still form occasionally.

BPO radicals can thermally degrade yielding a benzyl radical and carbon dioxide gas.

Furthermore, polymerization conducted in vials had to be slow to prevent high pressures from

pushing the top off. Slow polymerization is problematic for making composites because it

allows particles time to aggregate and settle.

Figure 13: A simple reaction vessel for polymerizing MMA at moderate pressures. The vessel is placed in the mouth of a c-clamp which can be tightened to increase the pressure inside the vessel.

To increase the polymerization rate without forming bubbles, pressure needs to be added. A typical high-temperature MMA polymerization process reported in the literature consists of heating to 74°C at 1000 psi.[12] However this required the use of molds and a high pressure bomb that would be very expensive to procure. Rather than operate at very high temperatures and hundreds of psi, experiments were conducted at moderately higher temperatures and a few psi using the reaction vessel shown in Figure 13. This vessel is made of three parts: cylinder, base and plunger. The cylinder is made of borosilicate glass tubing that is 1 inch O.D. and 1/16 inch thick. The base is machined aluminum fitted with a Viton® o-ring that is inert to MMA and seals with the glass to contain moderate pressures. The plunger is also machined aluminum fit with another Viton® o-ring. To maintain pressure, the vessel is placed in the mouth of a c-clamp. Tightening the clamp pushes the plunger down, decreasing the headspace above the polymerizing mass and thus increasing the pressure.

It was observed during experiments that the formation of large stagnant bubbles was preceded by very small bubbles which would quickly rise to the bulk surface and release into the headspace. This observation suggested that early in the polymerization process the viscosity of the bulk was low enough for these small bubbles to escape. A tiered heating schedule for polymerization was developed. Samples of 10g MMA with 10mg of BPO (BPO was obtained from Sigma Aldrich in a 50% weight mixture with dicyclohexyl phthalate) were placed in a 20ml

scintillation vial and heated, with stirring, to 90°C for 20 minutes. When small bubbles begin to rise to the surface, the sample was transferred from the vial to the reaction vessel in Figure 13. The clamp was tightened just enough to hold the plunger in place and the liquid level in the vessel was marked. The reaction vessel was then transferred to a 52°C oven.

The density of MMA (ρ=0.94) is significantly less than that of PMMA (ρ=1.19). As polymerization proceeds, the volume of the polymerizing mass decreases, creating a vacuum in the headspace that tends to pull bubbles out of the bulk. To counteract this, the c-clamp is tightened and the plunger lowered as the reaction proceeds. Typically the vessel had a headspace of about 5mm when it was placed in the oven. By reducing the headspace to about 2mm, a pressure of two or three atmospheres can be maintained in the vessel. After 4-5 hours in the 52°C oven, the samples were solid. They were typically left in the oven overnight and then cured for 2 hrs at 80°C the following morning. This procedure is good for producing homogeneous composites because it has a high initial reaction rate that quickly increases the viscosity of the bulk, thereby reducing settling. Furthermore it produces consistently clear PMMA, so that whatever scattering is observed in the composites can be attributed to embedded particles and not small bubbles.

B. Composites

To make a homogenous silica-PMMA composite, a surface agent is needed that can successfully bind the particle surface and be incorporated into the polymer matrix. As suggested in the literature these experiments used 3-(trimethoxysilyl)propyl methacrylate (3-TPM) as a coupling agent.[12] Figure 14 compares the structures of 3-TPM
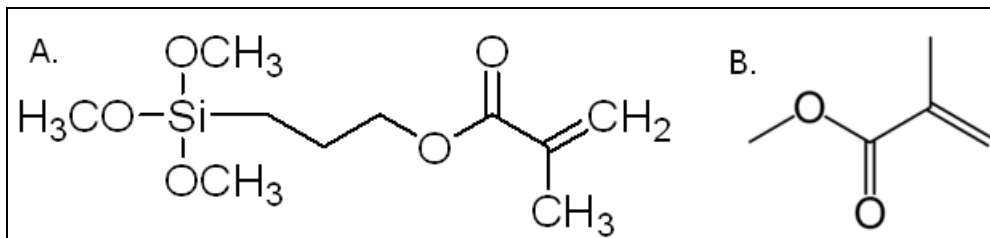
Figure 14: The coupling agent 3-(trimethoxysilyl)propyl methacrylate (a.) compared to methyl methacrylate monomer (b.)

and MMA. The right side of 3-TPM has the same structure as MMA, including the alkene bond through which polymerization proceeds, while the left side has an organosilicon moiety that can react with the silica surface by hydrolysis of the methoxysilane groups. 3-TPM anchors the silica particles and incorporates them into the PMMA matrix through covalent bonding.

Monodisperse spherical silica particles, made by the Stober method, were available in the laboratory from the previous work of Neal Abrams.[13,14] The particles used had diameters of 274 +/- 7.8nm, 350 +/- 20.7 nm, and 600 +/- 30.6nm. Particles were treated by sonicating 130mg particles in 35ml ethanol using a Branson Sonifier 250 for 15 minutes, adding 0.6ml of 3-TPM and vigorously stirring the dispersion for one hour. The particles were then dried using a vacuum filter with a polycarbonate membrane of pore size 30nm. The particles were washed three times by dispersing in ethanol and vacuum filtering. The clean 3-TPM coated particles were dispersed in MMA using a Branson 2510 sonicator for less than 3 minutes. The resulting dispersions displayed no noticeable settling over 20 min. The MMA-particle dispersions were polymerized as described in the procedure for neat polymer (Section A). Table 2 lists some important parameters for the composites obtained.

Table 2: Key parameters for experimentally produced composites

mass of polymer	10	10	10	10	10	10	g
mass of particles	15.0	2.0	10.3	2.3	10.0	50	mg
diameter of particle	274	350	350	600	600	600	nm
mean free path	256	2451	476	3654	841	168	μm
# scattering events	93.0	9.71	50.0	6.51	28.3	141	

A Hewlett Packard 8452A Diode Array Spectrophotometer was used to determine the

23

transmittance of the solar spectrum through the composite samples. The cylindrical samples

were placed on a stand at the same height as the photometer lamp. A ~2mm slit was placed in

front of the sample to eliminate lensing effects. Thus, the sample was approximately a rectangle

with a path length of one inch. The UV-visible was blanked without a sample present and all

measurements were made with the sample chamber closed to prevent ambient light from being

scattered through the samples. Figure 15 is a picture of the UV-visible set-up for measuring the

transmittance of composite samples.

Figure 15: A stand is placed in front of the UV-visible lamp to hold samples at the proper height. A cardboard slit approximately 2mm wide reduces the effects of lensing on the curved surface of the sample.

D. Thin Film Doped Silica

To evaluate the index refraction of titania and germainia-doped silicas, thin films of these materials were made and evaluated using UV-visible reflectance measurements.   To test a desired material composition the precursors, titanium (IV) butoxide, tetraethoxy germane and tetraethoxy silane were mixed in the desired molar percentages and added to alcohol so that the molar ratio of precursors to alcohol was 1:4. Binary mixtures of precursors in alcohol were dropped onto microscope slides, spin coated, and then baked on a hot plate at 400°C for 30 mins. This procedure was adapted from literature procedures for depositing thin layers of tin oxide.[15]

The resulting thin films were evaluated using optical microscopy to find defects. Defects included gaps, wavefronts, splash and droplet patterns, and burned regions. All of these defects would scatter light during measurements and lead to erroneous reflectance data. The procedure was optimized by adjusting the spinning speed and alcohol used. For both germania and titania doped silica, the best samples were obtained at a peak spinning rate of 2500rpm. Viscosity differences between initiators motivated a variation in the alcohol used for each. At room temperature the viscosity of titanium (IV) butoxide is 67 centistokes (cts), the viscosity of tetraethyl germane is 1.2 cst and that of tetraethoxy silane is 0.8 cst. The viscosity of ethanol is 1.5 cst and that of ispropanol is 2.5 cst. For germania-doped silica, ethanol produced uniform films with few defects. However, for titania-doping, thin films deposited from ethanol had varying thicknesses, wave fronts, and other defects. This was attributed to ethanol spinning off the slide quickly and leaving the much more viscous titanium (IV) butoxide behind. By mixing titania-doped silica precursor in isopropanol, which is more viscous, smooth films were obtained. For those films that displayed smooth surfaces, normal incidence reflectance data were obtained by holding the coated microscope slide perpendicular to the beam path in the UV-visible.

IV.   Results/Discussion

A. Polymer Composites

The data obtained from the UV-visible spectrophotometer is absorbance (A) vs.

wavelength (λ). Absorbance is converted to transmittance (T) by the following equation:

$$A = -\log_{10} T = -\log_{10}\left(\frac{I}{I_0}\right)$$

(5)

Absorbance represents the removal (scattering and absorbance) of light on a logarithmic scale. I

is the intensity of light that reaches the detector and I_o is the intensity of light that leaves the

lamp. The transmittance data for composite samples were normalized with respect to a neat

polymer sample. This allowed the affects of scattering particles to be isolated from issues of

lensing and surface reflectance. Silica has negligible absorption over the solar spectrum, so any

losses observed in the data result from scattering.[9]

Figure 16 shows the transmittance curves for particle loadings on the order of 0.001% by

mass. Mass of particles is held relatively constant, so the number of scatterers in the sample
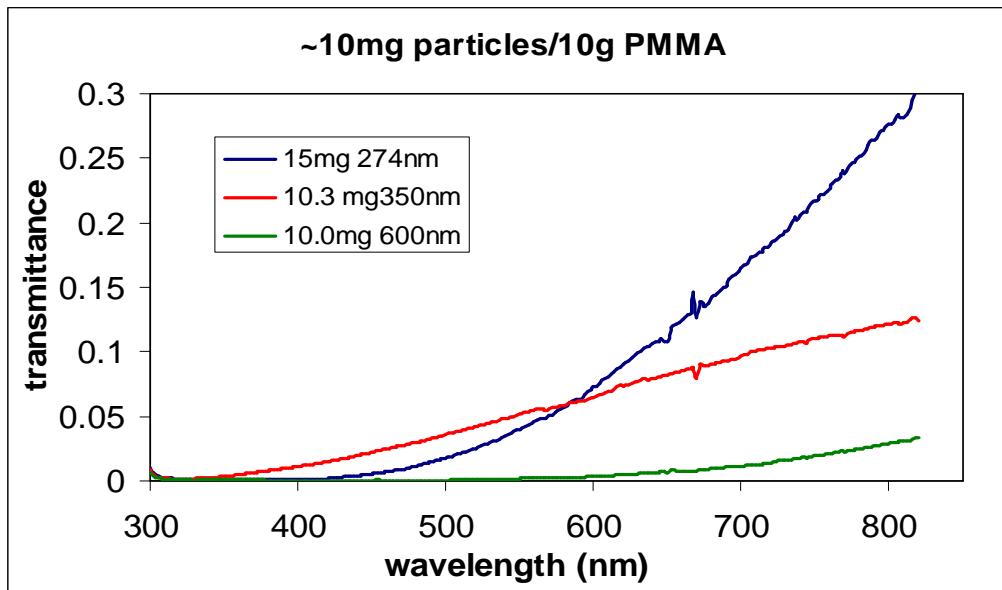

Figure 16: Experimental transmittance data for similar weight loadings of three particle sizes.

scales with the inverse of particle volume. Table 2 in the Experimental section shows the

average number of scattering events that occurs in each sample. The composite transmittance data agrees with many of the trends identified in Mie calculations. In Figure 16 for λ>600nm larger particles scatter more strongly despite the fact that there are fewer of them in the sample. This trend does not hold at lower wavelengths perhaps because the 274nm particles backscatter more. The 274nm particles display a fundamentally different shape in their transmittance curve. This could be attributed to the greater number of 274nm scatterers. Confirming this would require calculations of multiple scattering over populations of particles.

In Figure 17 the 0.0002% weight particle loading of 350nm particles displays a higher transmission that approaches what is required for the scattering lens. Again, the 600nm

2mg particles/10g PMMA

Legend:
— 2.0mg 350nm
— 2.3mg 600nm

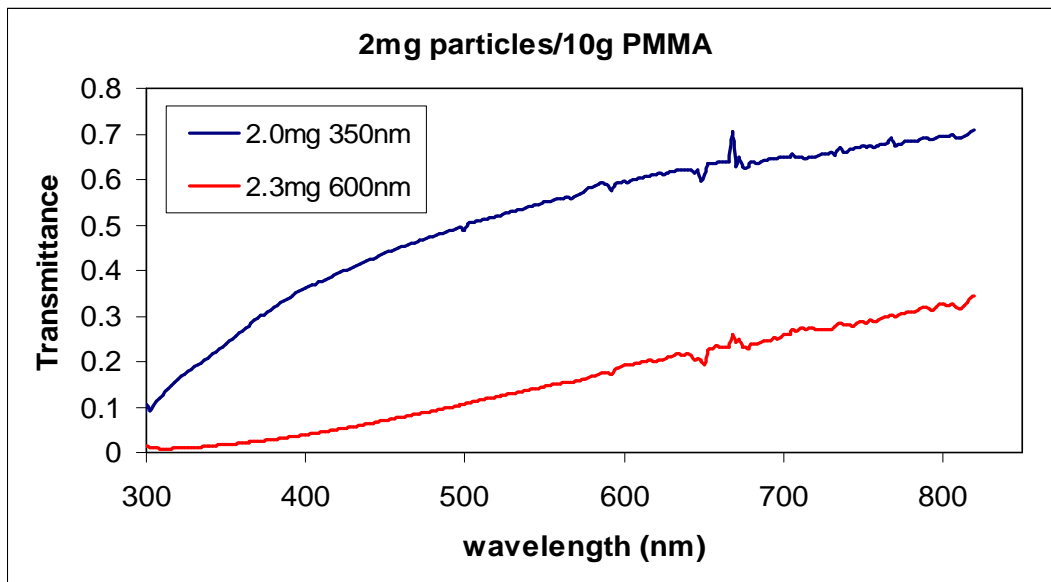x-axis: wavelength (nm)
y-axis: Transmittance

Figure 17: Experimental transmittance data for similar weight loadings of two particle sizes.

particles scatter more strongly and shorter wavelengths are scattered more strongly than longer ones. If the lens were made with 600nm particles, a weight loading of >0.0001% would likely be required. However, with index matching for λ>650nm the loading of 600nm particles in Figure 17 may be ideal as it scatters very strongly (presumably forward) for λ<650nm. It would be useful to see the transmittance data out to 1000 nm or so, but the UV-visible does not measure out to those wavelengths. Still, over a one inch path length the 350nm particles transmit nearly

70% for λ>650nm with a difference in index of refraction between particles and polymer of about 0.3 n. This is encouraging considering that 'index matched' composites from the literature transmits about 80% across this same λ range with a path length of only 0.25 inch.[12]

To better understand the scattering that is occurring in these silica-PMMA composites, transmission experiments should be conducted with a receiver that can move between 0° and 180° of the beam path. By collecting data at 20° degree intervals in between, it will be possible to assess the degree of backscattering, which should be greater for longer wavelengths. Also, such measurements would indicate how much multiple scattering deviates from the single scattering behavior predicted in the Mie Calculations. Furthermore, microscopy should be conducted to determine whether the silica particles are homogenously dispersed in the PMMA matrix. If the particles appear to be forming aggregates, different coupling agents, perhaps with more methacrylate moieties, should be investigated. Emulsion polymerization procedures, which encapsulate individual silica particles in polymer before polymerizing them into the larger polymer matrix, may provide for better separation between particles.[16]

With these additional experimental data it would then be useful to return to scattering theory. The Mie calculations made in Chapter 2 Section A apply to a single scattering event. While these calculations are useful for understanding the fundamental dependence of scattering on particle size, calculations should be made to determine the scattering that results from multiple scattering events as a photon propagates through the composite. Such calculations can be made by Monte Carlo simulations, which use the probability distribution of scattering angles from each individual scattering event to derive the total probability distribution for scattering through the entire silica-PMMA composite sample.[17] Free codes for running Monte Carlo simulations of Mie Scattering abound.[18]

B. Doped Silica

As is the case for the composite samples, the data obtained from the UV-vis for the thin-films is absorbance (A) vs. wavelength (λ). As before, transmittance is calculated from absorbance via Equation 5. For thin-films two major assumptions are made. The transmittance losses are assumed to come from reflection not scattering. Also, the reflection is assumed to occur at the interface between air and the doped-silica film and not at the interface between doped-silica and microscope slide. This is a decent assumption considering that the slide is made of borosilicate glass which should be relatively close in index to the doped-silica. These assumptions allow for the application of the Fresnel equation[19]:

$$n_f \quad = \quad \frac{1 + R + \sqrt{R}}{1 - R}$$

(6)

Here R is reflectance and n_f is the index of the doped silica. This form of the Fresnel equation applies only to normal angle of incidence from air (n~1.0) to some material.

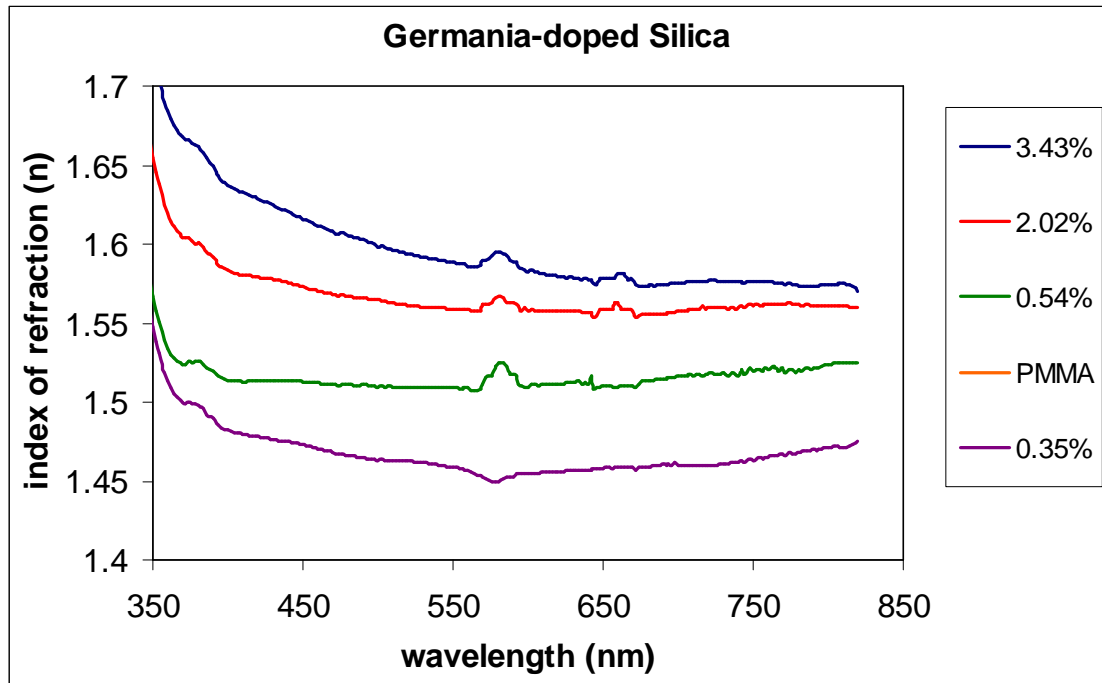The dispersion curves for various germania doping levels are shown in Figure 18. These

Figure 18: Index of refraction derived from reflectance data for various molar % of germania-doped silica

dispersion curves are very high compared to the ones calculated in Section C of Theory. Despite the smoothness of the films there is naturally some surface roughness that causes scattering and leads to overestimation of reflectance and n. The handbook of optical constants suggest that because n is so sensitive to errors in R, n values obtained using this methodology should be reported to only two significant figures. Though the exact magnitude of the germania-doped silica dispersion curves may not be correct, they do demonstrate that adding germania raises the index of silica fairly uniformly across the solar spectrum. Because the refractive index is overestimated due to defects and scales with the percent germanium doping, it seems that the amount of defects scales with germanium doping as well.

By comparison, titania-doped silica has a much steeper dispersion curve. Figure 19 shows the dispersion curves for titania-doped silica calculated in the same manner as Figure 19.
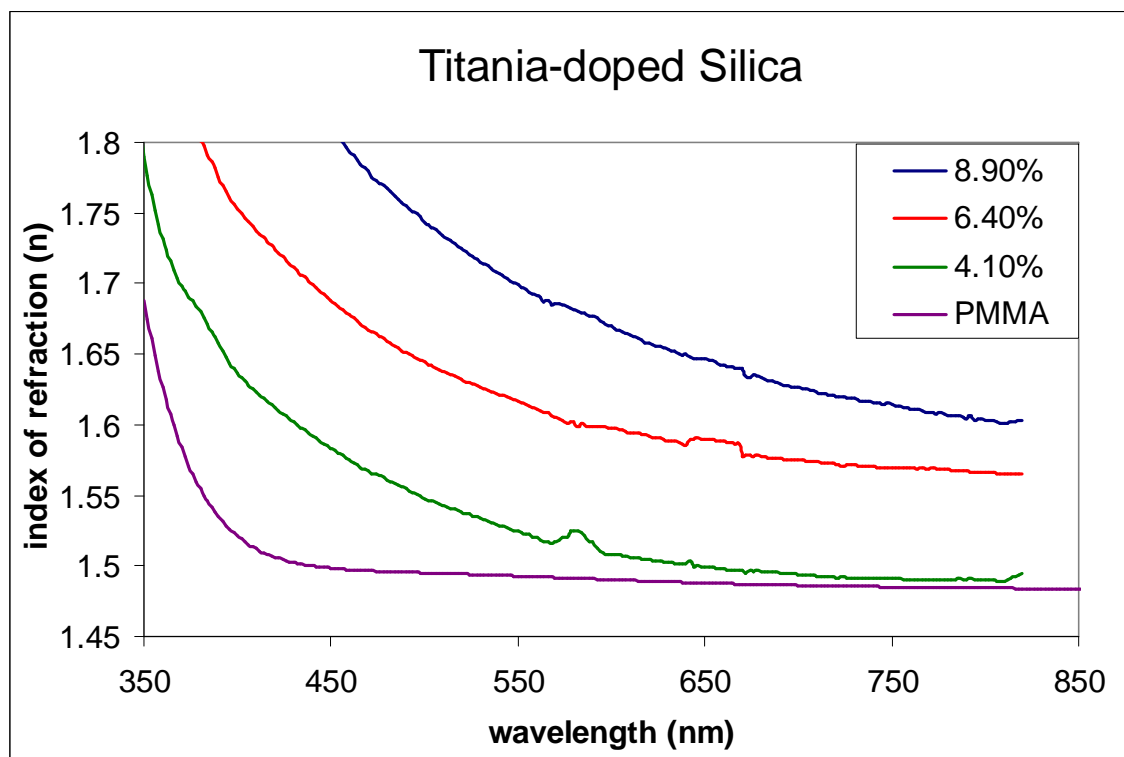

Figure 19: Index of refraction derived from reflectance data for various molar % of titania-doped silica

The curves rise quickly with increasing titania content and show increasing steepness in the low wavelengths. This fact could easily be exploited in pursuit of selective scattering. As the

steepness goes up in the blue region the blue wavelengths will be scattered more strongly. Whereas the flatness of germania-doped silica may be ideal for complete PMMA index matching, titania doped silica may be able to match PMMA in the red wavelengths only.

Producing spherical doped silica particles is the next experimental step in pursuing the selectively diffracting hybrid lens. Some attempts were made to synthesize doped silica particles via the Stober Method with germanium ethoxide and titanium (IV) butoxide precursors added, but TEM images of the particles revealed that they were extremely non-uniform in size, shape and composition. One main issue seems to be finding precursors that hydrolyze at equal rates so that particle formation can occur evenly. Unfortunately, no further experiments have yet been conducted on this issue.

Some research has been done on adapting sol-gel methods, like the Stober Method, to produce germanium-doped silica. Susa et al. used silcon methoxide and germanium tetra-methoxide solutions in water and hydrolyzed with ammonia solution to obtain silica gels doped with 0% to 20% germanium. They used bulk density as a proxy measurement for phase stability. Samples with higher bulk density were assumed to have germanium atoms more tightly integrated into the silica structure. They found that bulk density was at a maximum and the presence of residual hydroxyl groups was at a minimum when the metal precursor solution was hydrolyzed with an ammonia solution of pH=11.[20] A sol gel procedure such as this is a good first step for producing monodisperse germania-doped silica that could more closely match the refractive index of PMMA. If sol-gel methods fail to produce the uniform particles, core-shell procedures should be investigated.

V.   Conclusions

Hybrid solar cells have been proven to provide multiple band gap absorption of the solar spectrum. While this report is concerned with a DSSC/silicon hybrid, numerous combinations of solar cells could be employed in hybrid arrangements to achieve efficiency gains over single-junction cells. The selective light scattering needed for efficient solar conversion in the DSSC/silicon hybrid solar cell can be achieved using a lightweight and durable lens made of doped silica in PMMA. To produce forward scattering in the $\lambda < 650nm$, particles around 600nm in diameter should be employed. To prevent scattering in the $\lambda > 650nm$, dopants must be added to silica to increase its index of refraction and thereby match PMMA in this region of the solar spectrum. Germania and titania are two potential dopants though producing monodisperse spheres of silica that contain appreciable amounts of these dopants has not yet been accomplished.   This report presents a method for producing silica-PMMA composites that are cylinders one inch in diameter and free of bubbles. This composite is a model system for further study of selective light scattering.

VI. References

1. United States of America. Department of Energy. Energy Efficiency and Renewable
   Energy. Solar Energy Technologies Program. By Lawrence Kazmerski. Nov. 11
   2007.

2. Nelson, Jenny. The Physics of Solar Cells. London: Imperial College, 2004. Print.

3. "Solar Radiation Spectrum." Physics Department. Ben-Gurion University, 07 July
   2008. Web. 5 Apr. 2010. <http://www.bgu.ac.il/physics/>.

4. Brown, Gregory F. "Third Generation Photovoltaics." Laser and Photon Rev. 3.4
   (2009): 394-405. Web. 17 Nov. 2010.

5. "International Space Station Solar Power." Defense, Space and Security. Boeing.
   Web. 12 Mar. 2010. <http://www.boeing.com/defense-space/>.

6. "Clean-Energy Trends 2008." Clean Edge. 2008. Web. 07 Mar. 2010.
   <http://www.cleanedge.com/reports/reports-trends2008.php>.

7. Hoertz, Paul G. A Dye-sensitized Solar Cell - Silicon Photovoltaic Hybrid System.
   Tech. University Park, PA: Department of Chemistry and Materials Research
   Institute, 2008. Print.

8. Van De Hulst, H. C. Light Scattering by Small Particles. New York: John Wiley and
   Sons, 1957. Print.

9. Palik, Edward D., ed. Handbook of Optical Constants. 4 vols. Elsevier, 1998. Web.

10. Prahl, Scott. "Mie Scattering Calculator." Oregon Medical Laser Center. 2007. Web.
    Apr. 2010. <http://omlc.ogi.edu/calc/mie_calc.html>.

11. Olson, James R. "Fabrication and Mechanical Properties of an Optically Transparent
    Glass FIber/Polymer Matrix Composite." Journal of Composite Materials 26
    (1992): 1181-192.

12. Stoffer, J. O. "Preparation of Transparent Glass Fiber-reinforced PMMA Matrix

Composites." Polymeric Materials Science and Engineering 65 (1991): 221-22.

13. Stober, Werner. "Controlled Growth of Monodisperse Silica Spheres in the Micron Size Range." Journal of Colloid and Interface Science 26 (1968): 62-69.

14. Abrams, Neal M. Silica particle size data. Raw data. Penn State University Department of Chemistry, University Park, PA.

15. Demiryont, Hulya. "Optical Properties of Spray-deposited Tin Oxide Films." Applied Optics 26.18 (1987): 3803-810.

16. Bourgeat-Lami, Elodie. "Hybrid Silica/polymer Nanoparticles through Emulsion Polymerization." Materials Research Society Symposium Proceedings 628 (2000): 3.5.1-.5.7.

17. Plass, Gilbert N. "Monte Carlo Calculation of Light Scattering from Clouds." Applied Optics 7.3 (1968): 415-19.

18. "Mie Type Codes." ScattPort. Web. 19 Apr. 2010. <http://www.scattport.org/index.php/programs-menu/mie-type-codes-menu>.

19. Stapleton, Josh. "UV-Vis Basic Theory." Materials Characterization Lab. Penn State University. Web. 16 Apr. 2010. <http://www.mri.psu.edu/facilities/mcl/techniques/uv-vis/UV-VisTheory.asp>.

20. Susa, K. "Sol-gel Derived Ge-doped Siica Glass for Optical Fiber Applications." Journal of Non-crystalline Solids 119 (1990): 21-28.

Academic Vita

Education_____

The Pennsylvania State University, The Schreyer Honors College

B.S. in Chemical Engineering, with Honors in Chemistry
Minor in Economics

Graduation: May 2010

Research_____

IGERT: Summer Undergraduate Research Experience in Solar Hydrogen

Summer 2008
    University of Delaware, Department of Chemical Engineering

- Completed a 10-week program including undergraduate research and visits to local companies including Air Gas, BP Solar and Exxon Mobile Research.
- Worked under Chemical Engineering Professor, Dr. Jochen Lauterbach. Assisted a fourth year graduate student with the synthesis and evaluation of silver nanoparticles for the catalysis of ethylene epoxidation.
- Gained experience with UV-vis, SEM and TEM for materials characterization.

Penn State Biodiesel Research Group

Fall 2007-Spring 2008

- Member of the Biodiesel Undergraduate Research Group.
- Conducted Operations testing on a 50-gallon Biodiesel pilot plant using various feedstock oils, including canola, corn, soy and jatropha.
- Researched a method of converting free fatty acids into glycerides using Fischer Esterification, which is necessary for the conversion of used cooking oil to fuel.

Fall 2006-Spring 2007

- Undergraduate researcher for Chemical Engineering Professor, Dr. Joseph Perez.
- Researched fuel additives to improve cold flow properties of Biodiesel.

Presentations_____

"Differential Scanning Calorimetry and Photophysical Study of Interaction Between Quantum Dots and Polypropylene Matrix." Poster Presented at the Chemistry Department Spring Symposium, University Park, PA. April 29, 2009.

"Reverse Micelle Synthesis of Silver Nanoparticles for Ethylene Epoxidation." Poster Presented at the IGERT Energy and Sustainability Conference, Newark, DE. August 12, 2008.

"Penn State Biodiesel Research and Unit Operations." Poster Presented at EPA's P3 Sustainable Design Expo, Washington D.C. April 20-22, 2008.

Awards/Honors_____

- ❖ Dean's List 5/7 semesters
- ❖ Pennsylvania State University: The President's Freshman Award, February 2007
- ❖ AP Scholar with Honor, September 2006
- ❖ Walt Katuzny Memorial Scholarship, May 2006
- ❖ National Merit Finalist, May 2006